A method for detecting ionospheric disturbances and estimating their propagation speed and direction using a large GPS network

James L. Garrison,[1] See-Chen G. Lee,[1] Jennifer S. Haase,[2] and Eric Calais[2]

[1] A technique is developed for detecting short period (3–10 min) ionospheric disturbances and estimating their propagation speed and direction using data from a large GPS network (a hundred or more receivers). This method increases the signal-to-noise ratio of small signals and could be applied, autonomously, to process a large set of data for the study of the potential signal sources and statistical distributions of these disturbances. The integral electron content (IEC) for every satellite-station pair in the network is extracted from dual frequency phase data. These IEC time series are then band-pass-filtered and cross-correlated with each other. The resulting correlation power is an indication of the presence of a common disturbance recorded at the two stations, and the delay to the maximum correlation is a measurement of the propagation time between the ionospheric pierce points of the respective stations. A threshold on correlation power is used to select a subset of these delay measurements. The velocity of the detected perturbation is then estimated by fitting a two-dimensional plane wave model to this subset of measurements. A technique is developed to remove the effects of time-varying satellite motion and to reconstruct the waveform that would have been observed at a fixed point within the ionosphere. Consistency of the resulting velocity estimates is checked using a stacking-alignment method and a time-distance mapping that accounts for the motion of the GPS satellites. The sensitivity of the velocity estimate to both the assumed height of a thin-layer ionosphere and the detection threshold value is studied. A simulation is used to demonstrate the IEC waveform distortion due to satellite motion, and an example is shown in which this distortion is able to shift the dominant frequencies of an actual disturbance outside of the passband of the filter, thereby preventing detection. Four weeks of data, in different seasons, collected using the Southern California Integrated GPS Network (SCIGN), were processed. Over the total of 28 days, 127 significant disturbances were detected, most with horizontal propagation speeds between 50–1000 m/s and westward directions of propagation. A few cases with exceptionally high speed (>2000 m/s) were observed. It is hypothesized that these are manifestations of disturbances that occur simultaneously throughout the ionosphere, rather than traveling waves. The rate of occurrence of disturbances in the 3–10 min band was found to be larger than expected. Observational biases of this method are discussed.

[1]School of Aeronautics and Astronautics, Purdue University, West Lafayette, Indiana, USA.
[2]Department of Earth and Atmospheric Sciences, Purdue University, West Lafayette, Indiana, USA.

1. Introduction

[2] Perturbations in the height and electron density of the ionosphere have been studied for decades. The amplitudes of these disturbances are typically small

compared with the diurnal variation in the ionosphere. Use of a band-pass filter, combined with some test for signal coherence, is thus necessary in order to detect these disturbances in the presence of the much larger long-period variations.

[3] Short period (less than 10 min) disturbances, propagating near the speed of sound (700–1800 m/s), have been associated with shock acoustic waves generated by impulsive sources in the neutral atmosphere. Some sources include large earthquakes [*Calais and Minster*, 1995; *Afraimovich et al.*, 2001b; *Ducic et al.*, 2003; *Wolcott et al.*, 1984; *Otsuka et al.*, 2006], rocket launches [*Calais and Minster*, 1996; *Afraimovich et al.*, 2002; *Jacobson and Carlos*, 1994], large chemical explosions [*Calais et al.*, 1998; *Blanc and Jacobson*, 1989; *Fitzgerald*, 1997], and nuclear weapon tests [*Hines*, 1967].

[4] *Calais et al.* [2003] applied an array processing technique, using a 3–10 min band-pass filter, to GPS measurements from the Southern California Integrated GPS Network (SCIGN) [*Hudnut et al.*, 2001] to search for disturbances following the 16 October 1999 Hector Mines earthquake. Several waves were detected in that experiment. None of them, however, occurred at times that were compatible with the earthquake as a source. Those findings motivated the research which is presented in the present paper.

[5] The first step in determining the origin of these disturbances, which do not appear to be associated with known impulsive events in the atmosphere or the solid Earth, is to characterize the statistics of their occurrence.

[6] The following research was undertaken to develop an automated method for processing large sets of GPS measurements (one or more years) to detect these disturbances and estimate their speeds and directions of propagation. The time and propagation vector for individual disturbances could then be used to search for possible sources. A large ensemble of disturbances could also be studied to look for variations which are, for example, seasonally dependent or correlated with geomagnetic conditions.

[7] Dual-frequency GPS receivers are commonly used to measure the integrated electron content (IEC) through a linear combination of the pseudorange and carrier phase from the L1 and L2 frequencies (1575.42 MHz and 1227.6 MHz, respectively) [*Mannucci et al.*, 1998]. A network of hundreds of GPS receivers, such as SCIGN, provides for a dense sampling of the ionosphere and thus offers the possibility of detection and study of these disturbances through the optimal fusion of many measurements.

[8] Algorithms for the processing of an entire array of data must be computationally efficient, given the large number of stations presently available (250 in SCIGN). Thresholds for the detection of a disturbance and quality control of the data must be set autonomously to allow the

processing of data over a long period of time without operator intervention. Both of these requirements were important considerations in this research.

[9] One previously developed method for the detection of ionospheric disturbances in GPS data is the Statistical Angle-of-Arrival and Doppler Method (SADM-GPS) [*Afraimovich et al.*, 1998, 2000, 2003]. SADM-GPS computes the gradient in IEC measurements from three stations and projects this vector onto a two-dimensional plane to yield a time series of instantaneous propagation velocities. The velocity measurements are then time-averaged to reduce the noise and produce the propagation speed and direction, assuming a plane wave model. The detection threshold in *Afraimovich et al.* [2003] was based on the amplitude of the IEC variation. The width of the main lobe of the disturbance spectrum was used as a test of the quasi-monochromatic assumption.

[10] The method to be presented in this paper uses the cross-correlation between many pairs of IEC time series produced from receivers in the network. These cross-correlation measurements are constrained by a geometric model that is inverted to estimate the speed and direction of a propagating disturbance.

[11] The remainder of this paper is organized as follows: The method for estimating velocity from the filtered IEC time series is described in section 2. Section 3 introduces the statistical tests applied to determine the quality of the velocity estimate and the method for removing the effects of satellite motion to reconstruct undistorted IEC waveforms. Section 4 contains simulation results and sensitivity studies, and section 5 presents the experimental results. Section 6 compares the results in this paper with other published findings and makes recommendations on the use and limitation of our method for studying short-period disturbances in the ionosphere.

2. Data Processing

2.1. Generation of Filtered IEC Time Series

[12] We generated IEC time series from GPS data collected at a set of 175 stations within the SCIGN (http://lox.ucsd.edu) using the method described by *Mannucci et al.* [1993]. Only data sampled at 30 s intervals were used. The resulting IEC time series were passed through a fifth-order Butterworth band-pass filter with a passband between 0.0056 Hz and 0.0017 Hz (a period between 3 and 10 min) following the same approach as *Calais et al.* [2003]. An example of the raw and filtered IEC time series recorded at two stations is shown in Figure 1. In this example, one can see similar high-frequency signals in the time series from both stations. The maximum amplitude of the TEC disturbance can be seen to be approximately 2×10^{15} el/m^2 or 0.2 TECU.
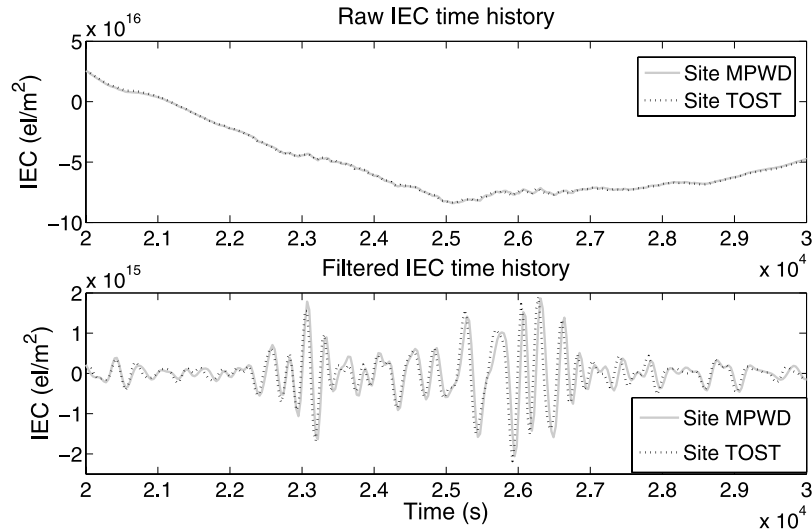
Figure 1. (top) Raw IEC time series, computed using the method from *Mannucci et al.* [1993]. (bottom) The same time series, after passing through the band-pass filter. The data are from satellite PRN27, observed at sites MPWD and TOST, on 7 July 2000. Observe that the high-frequency (filtered) component of the time series is very similar for both stations, but is delayed slightly for station MPWD.

[13] Variations observed in the IEC could be the result of changes in the concentration of electrons anywhere along the line of sight (LOS). We approximated the total change in the IEC as a change within a two-dimensional (2D) thin layer, located at a fixed altitude of 400 km (approximately the altitude of the F2 layer). The measurements of IEC variation were assumed to take place at the pierce point where the LOS from a GPS satellite to a receiver intersects this thin ionospheric layer. The projection of the pierce point onto the surface of a flat Earth will be referred to as the subionospheric point (SIP) in the remainder of this paper. The SIP locations were computed from the International GNSS Service (IGS) satellite orbits [*Kouba*, 2003]. Data from satellites with low elevations (<30°) were not used since this 2D representation is inaccurate in such cases. In section 4.2, we evaluate the sensitivity of the estimated propagation velocity to the assumed height of the thin layer. One consequence of this 2D approximation is that only the horizontal component of velocity is estimated.

[14] In Figure 2, filtered IEC time series are plotted, using color to indicate amplitude, along the corresponding SIP trajectories. An example data set for PRN27 on 7 July 2000 is shown in this figure. A strong perturbation is visible around 118°W longitude and 35°N latitude.

2.2. Cross-Correlation of Filtered Time Series

[15] We computed the cross-correlation between the normalized IEC time series from every pair of stations viewing the same satellite. This cross-correlation was used as a test for the presence of a coherent disturbance. Every IEC time series was normalized by its maximum amplitude. The unbiased, discrete-time cross-correlation function $C_{xy}[m]$ was then computed using the definition

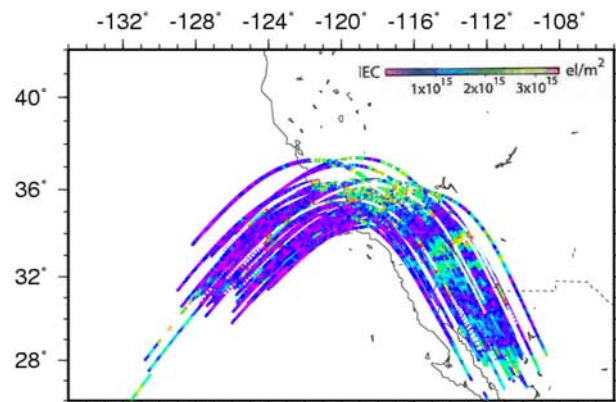$$C_{xy}[m] = \frac{1}{(N - ||m||)} \sum_{k=0}^{k=N-||m||-1} x[k+m]y[k] \qquad (1)$$

Figure 2. Map of the filtered IEC and the SIP trajectories between every station in the Los Angeles region and satellite PRN27, 7 July 2000. The disturbance magnitude is about 1.9e16 (*el/m²*).
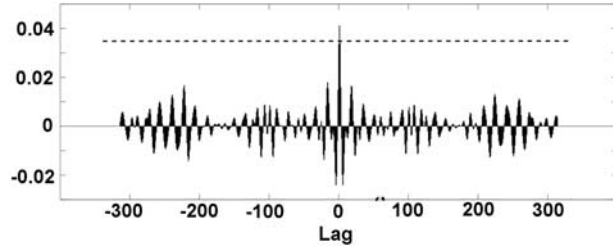
Figure 3. The cross-correlation between the two filtered IEC time series in Figure 1 (station MPWD and TOST). The horizontal line is the threshold. Lag is in discrete steps of 30 s.

in which $x[k]$ and $y[k]$ are discrete time series, m is the lag and N is the length of the series. Cross-correlation of many pairs makes it possible to identify coherent signals, even if their magnitudes are too low to be observed in the individual IEC time series.

[16] Figure 3 shows the cross-correlation of the two normalized IEC series shown in Figure 1. The lag, m_{max}, which produced the maximum amplitude of $C_{xy}[m]$ was used as a measurement of the time of travel between the SIPs corresponding to the two stations.

[17] We then tested the maximum of $|C_{xy}[m]|$ against a threshold. Exceeding that threshold would indicate the detection of a coherent signal in $x[m]$ and $y[m]$. In section 4.3, we study the sensitivity of the velocity estimate to the value of this threshold. The time delay, Δt_i, between the ith pair of stations, producing a $\max|C_{xy}[m]|$ above the threshold is $\Delta t_i = m_{max,i}T_s$. $m_{max,i}$

is the lag of the maximum $C_{xy}[m]$ and T_s is the sample interval of 30 s.

2.3. Estimation of the Propagation Velocity

[18] The forward model, relating the propagation velocity, $\vec{V}_p$ to the time-delay measurement, Δt_i, for the ith station pair, was based upon the simplified geometry in Figure 4. Note that $\vec{V}_p$ is the phase velocity of the ionospheric disturbance observed in the Earth-Centered-Earth-Fixed frame. In this model, the disturbance is assumed to be a plane wave, propagating at an assumed altitude, with a constant velocity, over a locally flat Earth. It is also assumed that only one disturbance is present within the time range and the geographical area studied. This method does not require the quasi-mono-chromatic assumption on the propagating ionospheric disturbances as in *Afraimovich et al.* [2003]. The disturbance waveform, however, was assumed not to change as it propagates over the network (i.e., it is assumed to be nondispersive).

[19] The displacement of the wavefront during the time Δt_i is the projection of the displacement vector between the SIPs corresponding to the two stations. The measurement Δt_i, produced from the maximum cross-correlation, can thus be related to the problem geometry and the unknown propagation velocity, $\vec{V}_p$, by

$$\Delta t_i = \frac{\Delta \vec{x}_i \cdot \vec{V}_p}{||\vec{V}_p||^2} \qquad (2)$$

which is the projection of the displacement between SIP's, $\Delta \vec{x}_i$, onto the direction of wave propagation, $\vec{V}_p$.
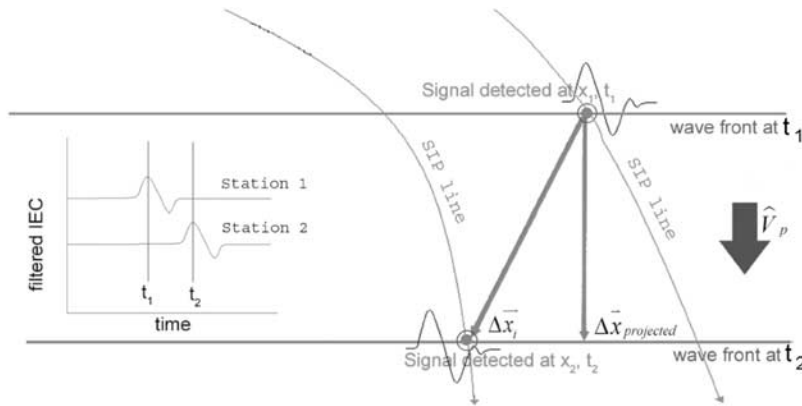
Figure 4. Geometry for deriving the forward model. At time t_1, the disturbance is detected at SIP location $\vec{x_1}$, for one of the satellite-receiver pairs. Sometime later, at t_2, a similar disturbance is detected at SIP location $\vec{x_2}$ for another receiver viewing the same satellite. If these two measurements represent detection of the same perturbation, observed at a different location in time and space, then the time difference between them is Δt_i, and the location difference is $\Delta \vec{x}_i$. Δt_i is determined from the lag which maximizes the cross-correlation, and $\Delta \vec{x}_i$ can be computed from the receiver locations and GPS ephemeris.

[20] Equation (2) can be written in a linear form as

$$\Delta t_i = \Delta x_{E,i} K_E + \Delta x_{N,i} K_N \qquad (3)$$

through a change of variables. (Subscript E and N denote the eastern and northern components of the vectors.)

$$K_E = \frac{V_{p,E}}{V_{p,E}^2 + V_{p,N}^2} \qquad (4)$$

$$K_N = \frac{V_{p,N}}{V_{p,E}^2 + V_{p,N}^2} \qquad (5)$$

[21] The components of $\mathbf{K}$ have a one-to-one relationship with the velocity components.

$$V_{p,E} = \frac{K_E}{K_E^2 + K_N^2} \qquad (6)$$

$$V_{p,N} = \frac{K_N}{K_E^2 + K_N^2} \qquad (7)$$

The displacement vectors, $\Delta \vec{x}_i$, were computed from the IGS orbits.

[22] The inversion of the model in equation (2) estimates $\mathbf{K} = [K_E \; K_N]$ from the set of measurements $\Delta \mathbf{t} = [\Delta t_1 \cdots \Delta t_n]^{\mathbf{T}}$. This was done using a linear least squares solution.

$$\widetilde{\mathbf{K}} = \left(\Delta \mathbf{x}^T \Delta \mathbf{x} \right)^{-1} \Delta \mathbf{x}^T \Delta \mathbf{t} \qquad (8)$$

where

$$\Delta \mathbf{x} = \begin{bmatrix} \Delta x_{E,1} & \cdots & \Delta x_{E,n} \\ \Delta x_{N,1} & \cdots & \Delta x_{N,n} \end{bmatrix}^{\mathbf{T}} \qquad (9)$$

[23] The matrix of residuals $\mathbf{R}$, for the estimate $\widetilde{\vec{V}}_p$, obtained from the estimate $\widetilde{\mathbf{K}}$, is given by:

$$R_i = \frac{\Delta \vec{x}_i \cdot \widetilde{\vec{V}}_p}{||\widetilde{\vec{V}}_p||^2} - \Delta t_i \qquad (10)$$

The estimated variance-covariance matrix of the parameters $\mathbf{K}$ was found from the residuals [Neter et al., 1996].

$$\mathbf{s}^2\{\mathbf{K}\} = \mathbf{R}^T \mathbf{R} \left(\Delta \mathbf{x}^T \Delta \mathbf{x} \right)^{-1} / (n - 2) \qquad (11)$$

[24] We used the covariance matrix $\mathbf{s}^2\{\mathbf{K}\}$, transformed to errors in $\vec{V}_p$, to assess the quality of the

estimate and produce error ranges on the maps of the velocity (section 5, Figure 18, for example).

3. Postprocessing, Visualization, and Quality Control

[25] We performed several postprocessing tests to assess the quality and consistency of our results. These include aligning the time series using the estimated velocity and a time-distance-IEC mapping (TDI map) which accounts for the motion of the SIPs during the time of the measurement. Stationary IEC waveforms were reconstructed by removing the distortions due to satellite motion.

3.1. Alignment Method

[26] We first applied an alignment method to visually demonstrate the existence of a coherent waveform in the TEC time series. A proper alignment of the time series would indicate a disturbance propagating at a velocity consistent with estimated results from the method in section 2.3. The stacking method in Calais and Minster [1996] assumed a disturbance propagating radially outward from a point. We modified this method to use the assumption of a plane wave.

[27] Let $\vec{D}_{sip}$ be the location of the SIP relative to an arbitrary point in north and east coordinates (assuming a flat Earth model). $\vec{D}_{sip}$ is projected into the direction of $\vec{V}_p$ to reduce the two dimensional problem to one dimension. The relative distance $D_R(t)$ from a reference position to each SIP, measured along the direction of propagation, $\hat{V}_p \equiv \vec{V}_p / ||\vec{V}_p||$, is therefore

$$D_R(t) = \vec{D}_{sip} \cdot \hat{V}_p \qquad (12)$$

[28] $\vec{D}_{sip}$, and thus $D_R(t)$, will change with time as a result of the orbital motion of the GPS satellites. The mean value, $\langle D_R \rangle$, found by averaging $D_R(t)$ over the time interval that a strong perturbation (amplitude above 50% of maximum) was present was used to generate a slant-stack plot. In this plot, each IEC time series, recorded at the ith station, is shifted by a lag of $\Delta t_{d,i}$

$$\Delta t_{d,i} = \frac{\langle D_R \rangle_i}{||\vec{V}_p|| - \vec{V}_{sip,i} \cdot \hat{V}_p} \qquad (13)$$

in the time axis (abscissa) and by the projected distance $\langle D_R \rangle$ in the vertical axis (ordinate).

[29] Figure 5 is an example of aligned plot for 7 July 2000. It can be seen that most of the waveforms appear to be similar to each other, thus visually confirming the detection of a common disturbance observed by all stations in the array. Following the shift in time from equation (13), the disturbances from all stations are also
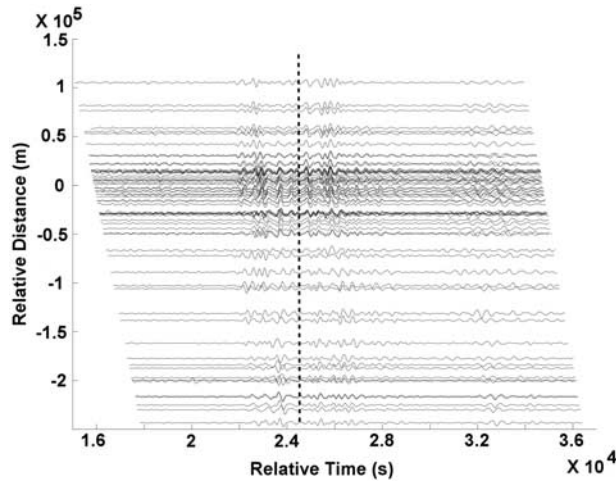
Figure 5. Aligned plot of the IEC time series for PRN27 on 7 July 2000. The abscissa (x) is the time, shifted by Δt_d from (13), and the ordinate (y) is the projected distance $D_{R,m}$ along the propagation direction. Observe the similarity between the waveforms, and their approximate alignment in time (represented with the vertical dash line). Only time series producing correlation values above the threshold (and thus used in the velocity estimation) are shown on this plot.

propagation. The slope of the coherent patterns in the colors is equal to the propagation speed of the disturbance. This slope must be positive and the similar colors (i.e., wavefronts) must be aligned for the data to be consistent with the estimated velocity. The TDI map thus provides an additional qualitative test of both the existence of a coherent IEC waveform and a reasonable estimate of its propagation velocity.

3.3. TDI Map of Multiple Satellites

[32] Data from multiple satellites can be plotted on the same TDI map. Figure 7 shows the filtered IEC time series from PRN8 (the upper stack) and PRN27 (the lower stack). A disturbance is present in the signals from both satellites at an approximate time of 6–8 H UTC and the IEC variations show similar slopes in the color patterns that align with each other. Therefore we conclude that the same disturbance was observed in the signal from both satellites.

[33] The TDI map in Figure 7 also shows that some parts of the waveform has attenuated or strengthened over time. The IEC waveform and propagation velocity may change over time, as shown in Figure 8 in which the data from an additional satellite (PRN2, the upper stack)

approximately aligned in this new time reference. This confirms that the propagation velocity estimated from the cross-correlation method in section 2.3 is consistent with the measured data.

3.2. Time-Distance-IEC Mapping

[30] Next, we combined the SIP map from section 2.1 with the alignment method described in section 3.1 above. In this time-distance-IEC (TDI) plot, the x-axis (abscissa) represents the time (not shifted) and the y-axis (ordinate) represents the time-varying distance projected onto the direction of propagation to each SIP point, $D_R(t)$. We ploted each IEC time series, using a color scale to represent normalized signal amplitude, at the appropriate points along the SIP trajectory. The difference between this method of visualization and the alignment method is that the time-varying $D_R(t)$ accounts for the motion of each SIP whereas, on the stacking-alignment plot of Figure 5, the SIP locations are approximately placed at the average distance $\langle D_R \rangle$.

[31] Figure 6 shows an example of a TDI plot, in which the parallel lines of similar color demonstrate that the IEC variations observed at multiple receivers are coherent. The slope of each SIP trajectory in the $t - D_R$ plane is equal to the component of the SIP velocity (due to satellite motion) projected onto the direction of

Figure 6. Time-distance-IEC (TDI) map of PRN27, 7 July 2000. The slope of the aligned color (representing filtered IEC) is the propagation speed. The reconstruction method (section 3.4) projects all normalized IEC time series onto the solid line (i.e., the "screen") and then transforms them into a coordinate along the dashed line, which is parallel to the time axis. Only time series producing a correlation value above the threshold are shown on this plot.
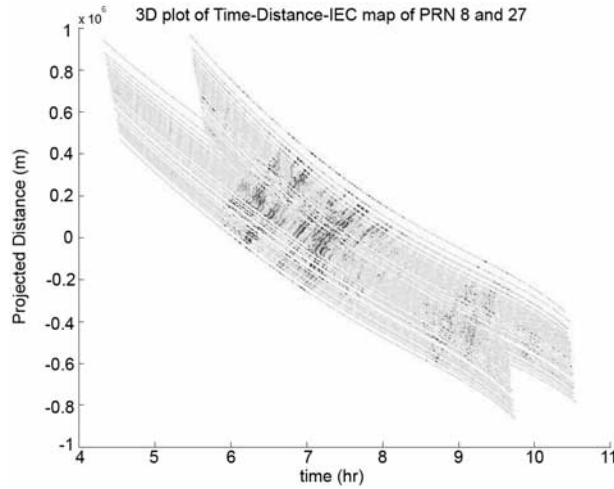
Figure 7. Time-Distance-IEC map of satellites PRN8 and PRN27 showing detection of the same propagating disturbance on 7 July 2000. Only time series producing correlation values above the threshold are shown on this plot.

is added and it is seen the colors do not align well with the patterns in the signal from satellites PRN8 and PRN27.

3.4. Reconstruction of IEC Waveforms

[34] In the results presented in this paper only measurements from one satellite, recorded at multiple ground receivers, were processed together to produce a velocity estimate. All of the SIP trajectories from the same satellite would have a very similar path, as can be seen in the SIP maps in Figure 2. This is a consequence of the large distance to the satellite, relative to the separation between receivers. Distortion of all of the waveforms would be very similar and thus would not significantly affect the cross-correlations.

[35] We used a transformation to remove the time-varying SIP motion from the IEC time series and produce a waveform which represents the measurement that would have been made at a fixed point in the thin ionospheric layer.

[36] The general description of the variation in filtered IEC with the motion of the corresponding SIP is a four dimensional problem (IEC, time, and the SIP location in two dimensions, $\vec{D}_{sip}$). The assumption of a plane wave propagating with a constant velocity, $\vec{V}_p$, reduces this problem to two dimensions (IEC and a transformed time-distance variable). The location of the SIP was projected onto the direction of the propagation velocity. The independent variables of time and D_R, used in the TDI map, can then be transformed to a new set of orthogonal coordinates. One of these new coordinates is aligned in the direction of $\hat{V}_d$ as shown in Figure 6. The unit vector

$\hat{V}_d$ is the direction of the coherent color pattern on the TDI map. All IEC values on the TDI map can be projected into the "screen" of $\hat{V}_{d\perp}$. This "screen" slides along the direction of $\hat{V}_d$, illustrated in Figure 6.

[37] This coordinate transformation is described mathematically as:

$$DT_{proj} = [t \ D_R] \cdot \hat{V}_{d\perp} \qquad (14)$$

where $[t \ D_R]$ is a two-element-vector, which consists of scalar t and scalar D_R. The filtered IEC was plotted against the transformed time-distance variable, DT_{proj}. Every IEC time series, from a different SIP, should overlap when plotted against DT_{proj} and could then be averaged to reduce noise. The stacked waveform can then be transformed into an equivalent waveform as would be measured at a fixed location in the ionosphere, through scaling the x-axis by

$$t_{new} = \frac{DT_{proj}}{\hat{x}_t \cdot \hat{V}_{d\perp}} \qquad (15)$$

where $\hat{x}_t$ is a unit vector in the direction of the time axis on Figure 6.

[38] After applying this scaling to the independent variable DT_{proj}, the resulting plot of IEC versus t_{new} has dimensions of normalized IEC (non dimensional) and time, respectively.

[39] Figure 9 shows the reconstructed IEC time series for PRN27, from the data recorded on 7 July 2000. The
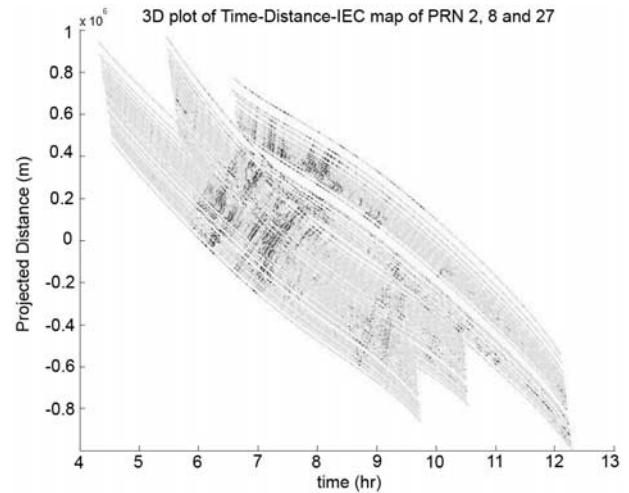

Figure 8. Time-Distance-IEC map of satellites PRN2, PRN8 and PRN27 showing detection of the same propagating disturbance on 7 July 2000, but the disturbance appears to have distorted before reaching PRN2 (the upper plot). Only time series producing correlation values above the threshold are shown on this plot.
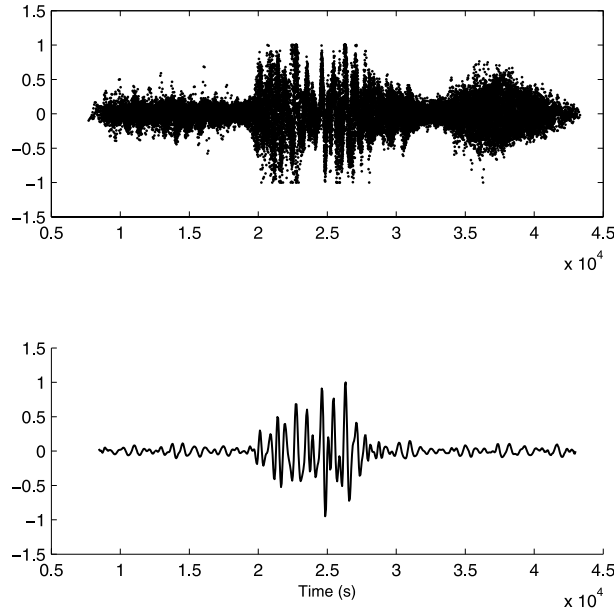
Figure 9. Reconstructed IEC waveform from PRN27 on 7 July 2000, removing the effect of SIP motion. IEC time series are shown as points and averaged to produce the lower plot. This waveform represents a measurement that would be obtained by a sensor at a fixed location in the ionosphere. As can be seen in this figure, the filtered time series from all ground stations are very similar, indicating a coherent disturbance.

time series from all stations, once transformed, appears to be very similar, further confirming the presence of the same disturbance propagating over the network (as long as dispersion is insignificant). These waveforms can then be averaged, as shown on the lower plot in Figure 9, to generate a model waveform for the disturbance with the effects of satellite motion removed.

4. Simulation and Sensitivity Studies

[40] In this section, we use simulations to demonstrate the Doppler-like effect from satellite motion and show how this could influence the ability to detect a disturbance. We also present studies of the sensitivity of the estimated propagation velocity to the ionospheric height assumption and to the threshold of detection.

4.1. Simulation of the Doppler-Like Effect

[41] A simulated IEC time series was generated from

$$
\begin{aligned}
IEC(\vec{R}, t) = {}& \mathrm{sinc}\left[\omega_{bw}\left((t - t_d) - \frac{(x - x_d)}{V_p}\right)\right] \\
& \cdot \cos\left[\omega_c\left((t - t_d) - \frac{(x - x_d)}{V_p}\right)\right]
\end{aligned} \tag{16}
$$

in which $\vec{R}$ is the 2D SIP position and x is the distance along the wave propagation direction ($x = \hat{V}_p \cdot \vec{R}$). An arbitrary reference point is denoted with subscript d. ω_c is the central frequency (8.1×10^{-3} rad/s) and ω_{bw} is the bandwidth (5.4×10^{-4} rad/s).

[42] A simulation, using the synthetic IEC disturbance in equation (16), was used to demonstrate the distortion of the IEC signal resulting from the movements of the SIPs. The results of this simulation are shown in Figure 10. The left plot shows the simulated waveform and the power spectrum of the signal recorded at a fixed position. The middle plot shows the distorted waveform and power spectrum that would
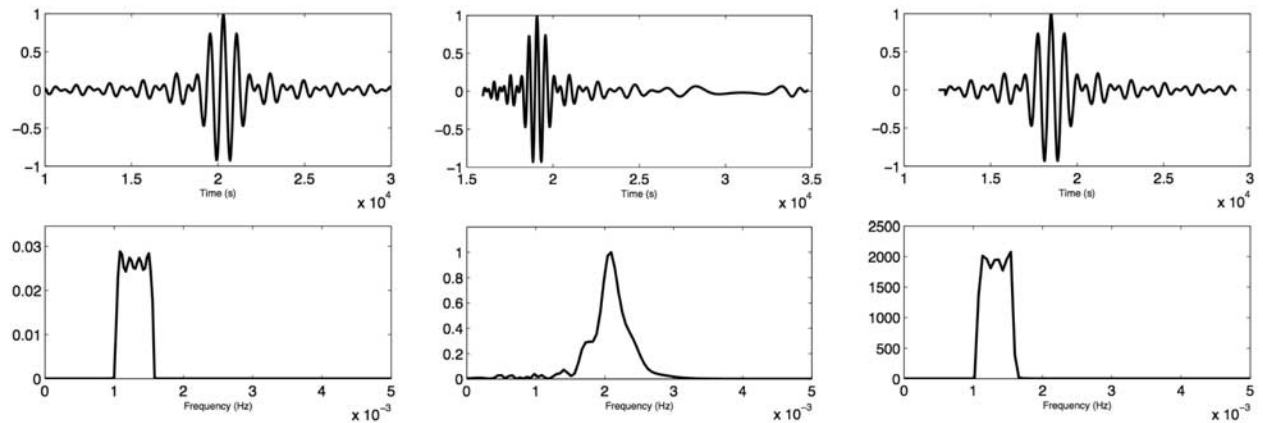

Figure 10. Simulated IEC waveforms. (left) The IEC waveform recorded in a fixed position. (middle) The same IEC disturbance observed along the SIP trajectory. (right) Reconstructed IEC waveform from the distorted IEC waveform.
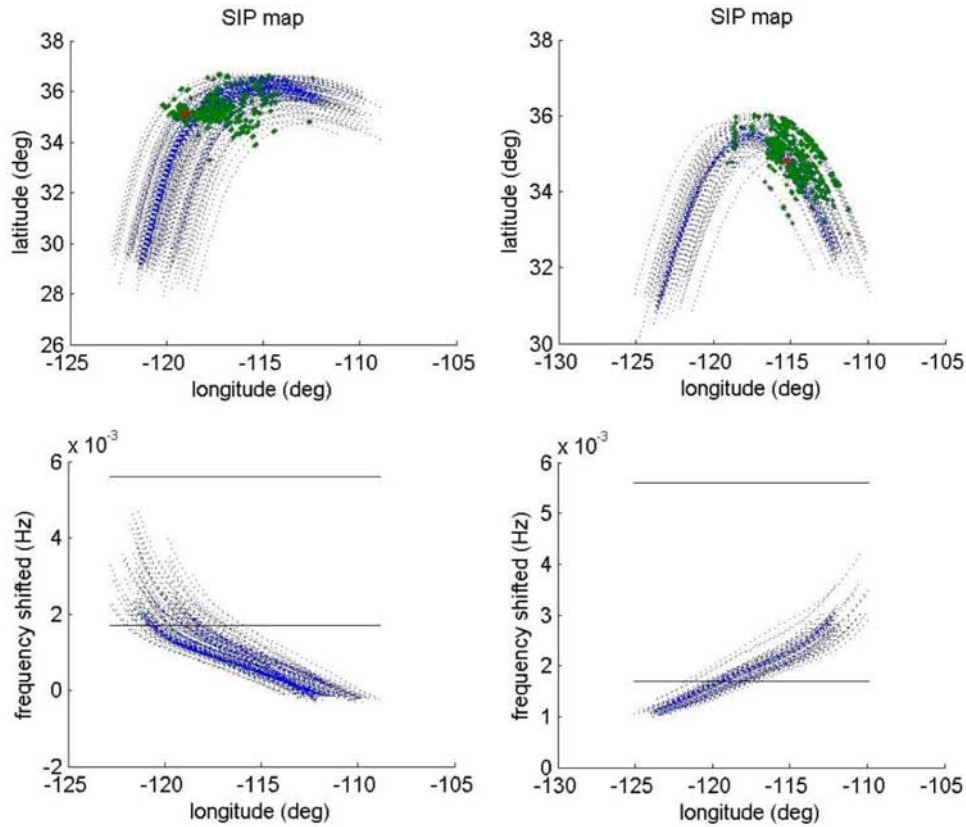
Figure 11. (bottom) Estimated shift of central frequency for PRN29 on 18 October 2001 on the left and for PRN19 on 7 July 2000 on the right. The two horizontal lines represent the upper and lower bound of the 3–10 min filter. (top) The dotted-lines represent the SIP trajectories of PRN29 and 19, the location of detected strong disturbance are plotted with heavy dots. No disturbances were found in the PRN29 data until the filter bandwidth was widened to 2–20 min. With the wider bandwidth, a disturbance was detected in agreement with the results in *Afraimovich et al.* [2003] The upper plot for 18 October 2001 shows the detections after the filter bandwidth was increased to 2–20 min.

have been recorded from a moving SIP using the data for PRN27 on 7 July 2000. The right plot shows the waveform reconstructed from the distorted one using the method described in section 3.4.

[43] The distortion due to this relative motion is significant since the speed of the SIP is usually in the range of 50–300 m/s, which is within an order of magnitude of the speed of many ionospheric disturbances.

[44] We will refer to this as a "Doppler-like" effect to distinguish it from the more common Doppler effect on the GPS carrier frequency due the satellite-receiver motion. The frequency shift Δf_p of a monochromatic wave with a frequency of f_p at rest is given by:

$$\frac{\Delta f_p}{f_p} = -\frac{\vec{V_{sip}} \cdot \vec{V_p}}{||\vec{V_p}||^2} \qquad (17)$$

[45] Different satellites have different SIP velocities, thus the distortions of recorded IECs for the same ionospheric disturbance would appear to be different. As discussed in section 3.4, this distortion should not significantly affect the cross-correlation between the signals from the same satellite received at multiple ground locations that are close together.

[46] In this section, we consider the possibility that the Doppler-like effect, for some viewing geometries, would shift the disturbance spectrum outside of the passband of the precorrelation filter. This is evaluated as one possible reason for the detection of a disturbance in some, but not all, SIPs within the same spatial area and time frame.

[47] Figure 11 shows the shift in the central frequency (approximated as the average frequency in the 3 dB bandwidth) of two different cases of IEC perturbations, using the SIP trajectories for PRN29 on 18 October 2001 and PRN19 on 7 July 2000. A perturbation was detected
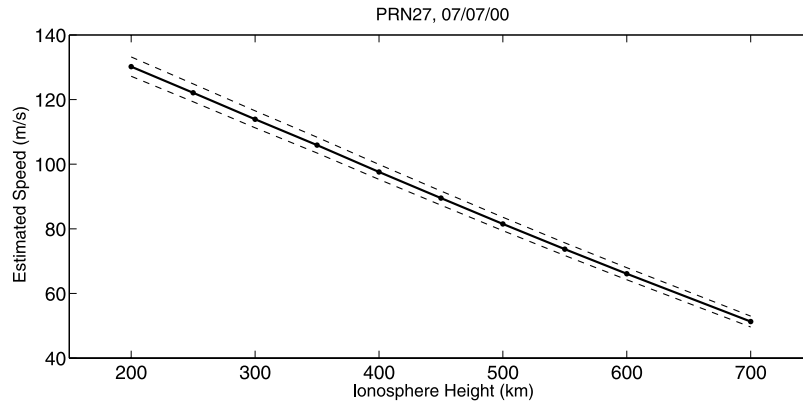
Figure 12. Sensitivity of the estimated propagation speed to the assumed height of the thin-layer ionosphere. Data for PRN27 on 7 July 2000. The upper and lower lines represent the boundary of 2 STD of error.

in measurements from PRN19 on 7 July 2000, using a filter bandwidth of 3–10 min.

[48] The case of PRN29 on 18 October 2001 is significant. *Afraimovich et al.* [2003] reported the detection of a disturbance propagating south–east on 18 October 2001, using the SADM-GPS technique on PRN29. No such perturbation was found by using our cross-correction method with a 3–10 min bandwidth.

[49] The two lower plots show the expected distortion of the signal along the SIP maps plotted above them. These plots shows that the SIP trajectories of PRN19 are such that the SIP motions keep the relatively strong ionospheric disturbance (visible between longitudes of −120° to −115°) within the bandwidth of the filter. However, the frequency shift for PRN29 moves the central frequency outside of the 3–10 min bandwidth, when the SIP positions are between longitudes of −120° to −110°. Therefore, a possible explanation for the lack of a detection on 18 October 2001 is that the filter has attenuated a significant portion of the signal. This was indeed found to be the case. An IEC disturbance can be observed in the signal from PRN29 once the filter passband is widened to 2–20 min. The estimated speed and azimuth of this disturbance are 162.7 m/s and 162.3°, comparable to the numbers reported by *Afraimovich et al.* [2003] of 190 m/s and 140°.

[50] Widening the bandwidth for all searches, however, would introduce more noise into the TEC time series. Therefore we will continue to use a 3–10 min passband for the remainder of this paper. A systematic search for disturbances, using this method, could be done with a bank of filters that have overlapping, narrow, passbands.

[51] Finally, it should be noted that the Doppler-like shift in frequency is not constant over time, thus we cannot reconstruct the signal by simply shifting the power spectrum. The waveform must be corrected using the time-varying geometry as was described in section 3.4.

4.2. Sensitivity to the Ionospheric Height Assumptions

[52] We had assumed a height of 400 km for the thin layer approximating the location of the ionospheric disturbance. Other researchers have used different numerical values (e.g., 300 km in *Afraimovich et al.* [1998]). In order to study the sensitivity of the estimated velocity to the assumed altitude, we ran the estimator on the data from PRN27 on 7 July 2000 using a range of heights from 200 to 700 km.

[53] These results are shown in Figures 12 and 13. The estimated speed depends almost linearly on the height assumption, with a decrease of approximately 15 m/s per 100 km of height. The error bars show the range of 2 standard deviations (STD) of uncertainties computed from equation (11). The estimated propagation direction does not significantly change (less then 1 degree) with variation in the height assumption as shown in Figure 13.

4.3. Sensitivity to the Detection Threshold

[54] The propagation velocity estimate from the linear least squares problem in section 2.3 was found to be sensitive to the threshold set for accepting measurements.

[55] The quantity that we chose for the threshold test was the correlation strength normalized by the standard deviation of the cross-correlation. In essence, this is a signal-to-noise measurement.

$$S/STD = \frac{|\max(C_{xy}) - \mathrm{mean}(C_{xy})|}{\mathrm{std}(C_{xy})} \quad (18)$$
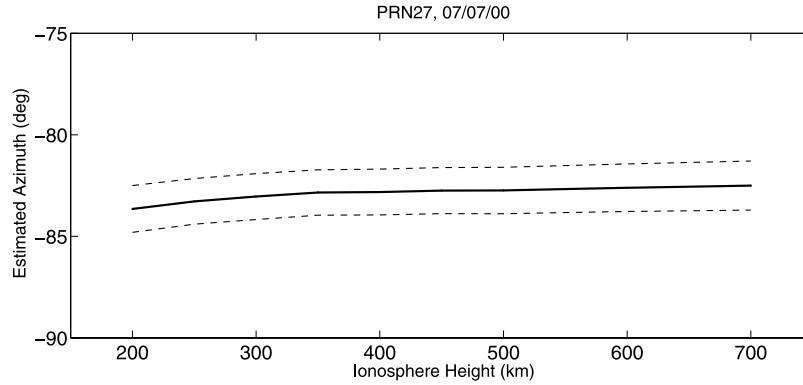
Figure 13. Sensitivity of the estimated propagation direction to the assumed height of the thin-layer ionosphere. Data for PRN27 on 7 July 2000. The upper and lower lines represent the boundary of 2 STD of error.

[56] We varied the threshold for *S/STD* and examined the quality of the resulting estimates using three metrics. The efficiency of the linear model allowed the estimator to be run using several sets of data from different thresholds of *S/STD*. The appropriate threshold was selected by applying three tests to the quality of the resulting estimate.

[57] The first metric was based on the predicted error from the estimator. We divided the size of the error ellipse described in section 2.3 by the magnitude of the estimated parameter $\|\mathbf{K}\|$ to represent the estimation error as a percentage:

$$\text{error}\,\% = \frac{\sqrt{\lambda_1^2 + \lambda_2^2}}{\|\mathbf{K}\|} \times 100\,\% \qquad (19)$$

The eigenvalues λ_1 and λ_2 of the estimation covariance matrix $\mathbf{s}^2\{\mathbf{K}\}$ are the semimajor and semiminor axes of an error ellipse containing one standard deviation of possible estimates.

[58] The covariance matrix $\mathbf{s}^2\{\mathbf{K}\}$ only describes the distribution of estimates about their mean. A quality estimate would also produce estimation residuals (from equation (10)) that are close to zero mean. In other words, the estimate should be unbiased. The second metric, therefore, was the magnitude of the mean of the residuals. They were usually found to be below 7.5 s.

[59] The third test metric was the standard deviation of the residuals. This quantity was usually below 50 s. In considering the numerical thresholds set for these two metrics, recall that the delay measurements obtained from the discrete cross-correlation are quantized by the 30 s sampling rate of the GPS receivers. That quantization value will set the lower bound on the uncertainty of an individual delay measurement.

[60] The threshold on *S/STD* was set to meet all three of the following criteria: error% smaller than 50%; mean residual below 7.5 s; and standard deviation of the residuals less then 50 s. Estimates of the propagation velocity were extracted for each day, varying the threshold *S/STD* from 2.5 to 7.0 in steps of 0.1. Any value of *S/STD* which produced results meeting all three of these criteria was deemed acceptable. In most cases, we found a wide range of threshold values which met these criteria. All produced very similar estimation results.

[61] In Figure 14, we plot the error% and the mean residuals as functions of the threshold *S/STD* for the data from PRN27 on 7 July 2000. The solid lines represent error% and the dots represent mean of residuals. The top plot shows the performance versus the percentage of IEC-time series pairs included in the estimate. The bottom plot shows the performance versus the *S/STD* threshold. This figure clearly shows the thresholds between *S/STD* of 3.9 to 5.5 are acceptable. With a threshold set higher than this range, few measurements are included in the estimation, whereas for a threshold below this range, too many noisy measurements are included. Both extremes would degrade the quality of the velocity estimation. Given that the linear least squares solution in equation (8) can execute very quickly and that the threshold value can be tested in large steps (since the sensitivity is weak) a range of *S/STD* thresholds were used for each data set. Any thresholds would likely give acceptable velocity estimates, as long as it satisfied all three criteria above.

4.4. Data Quality Control and the Detection Threshold

[62] We did, however, observe a few anomalous cases in which a small change in *S/STD* threshold, such as to include a single additional delay measurement, could

Figure 14. The dependence of velocity error (error%) and the mean of the residuals on the detection threshold. Data for PRN27 on 7 July 2000. The solid lines represent error%, and the dots represent mean of residuals. (top) Performance versus the percentage of IEC-time series pairs included in the estimate. (bottom) Performance versus the S/STD threshold (equation (18)).

produce substantial changes in the estimated velocity and direction, as well as large changes in the three metrics described above. In this section, we investigate the cause of these anomalous delay measurements. Individually, some of these outliers did have high S/STD, so that if they are rejected strictly on the tests described in section 4.3, many good measurements would also be rejected.

[63] Referring back to Figure 4, observe that as the wavefront moves between times t_1 and t_2 (i.e., Δt_i positive), all $\Delta \vec{x}_i$ should appear in the same half-plane. Thus, we can plot the projected observation velocity $\vec{V}_{ob,i} = \Delta \vec{x}_i / \Delta t_i$ and check that the directions of all $\vec{V}_{ob,i}$ are in the same half-plane. For example, Figure 15 (PRN8, 7 July 2000) shows that all $\vec{V}_{ob,i}$ appear in the half-plane to the left
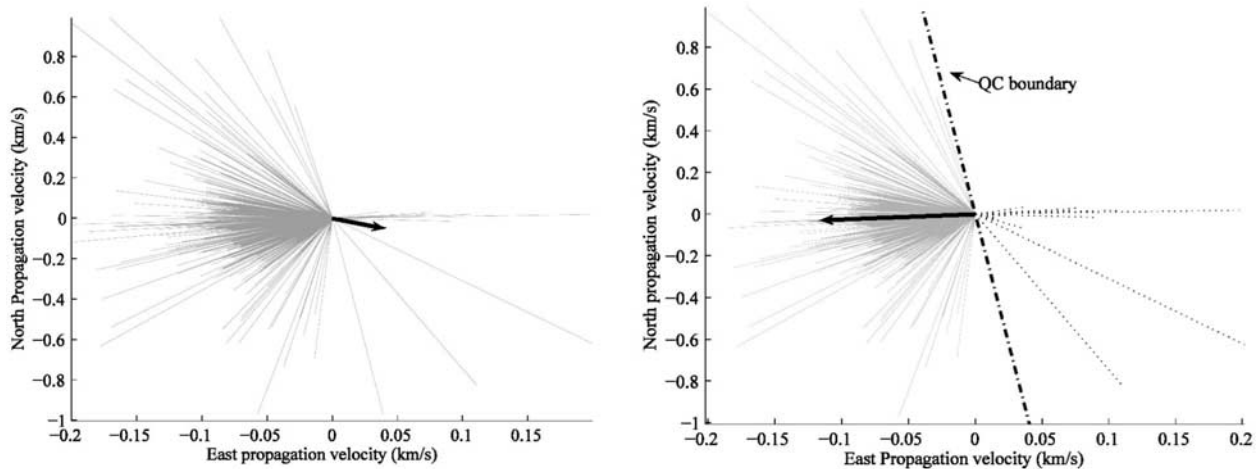
Figure 15. Plot of the projected velocity $\vec{V}_{ob}$ of satellite PRN8, 7 July 2000. (left) Most of the $\vec{V}_{ob}$ are pointing in the same half plane except for a few outliers, which cause the least squares solution (the thick vector) to give erroneous results. (right) A "quality control" (QC) boundary is set to separate the outliers from the correct $\vec{V}_{ob}$. Once the outliers are removed by this method, the least squares solution (the thick vector) is acceptable.
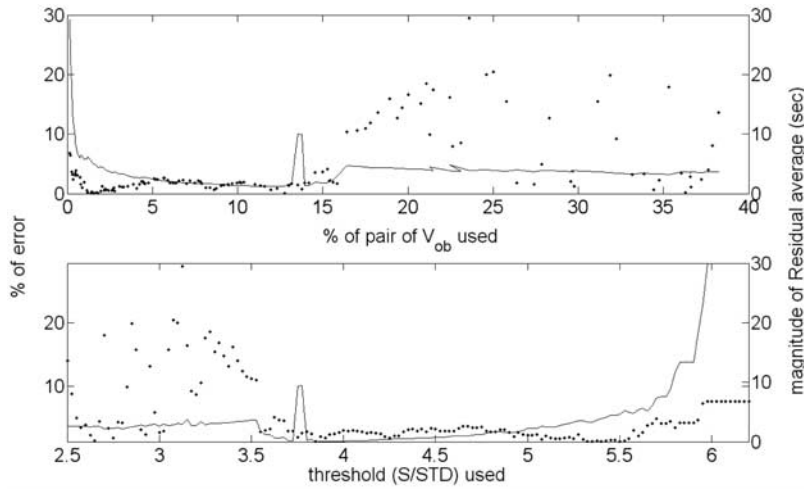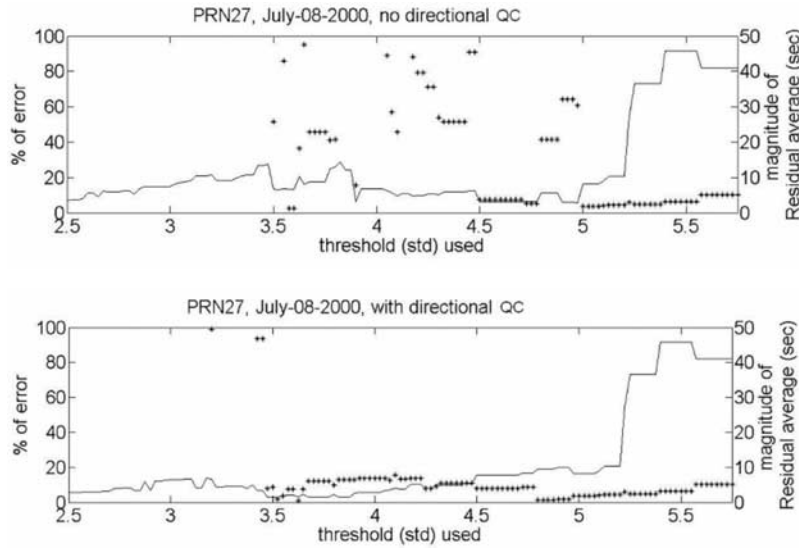
Figure 16. The dependence of velocity error (error%) and the mean of residuals on the detection threshold, S/STD, for PRN27, 8 July 2000. (top) Performance without data quality control; (bottom) performance with data quality control.

of the "QC (Quality Control) boundary," with the exception of a few outliers.

[64] The QC boundary test was applied to eliminate these outliers prior to the least squares estimation. The orientation of the QC boundary is selected so that the least number of $\vec{V}_{ob,i}$ are outside of the half-plane. Those remaining outside of the half plane are considered to be outliers and will be excluded from the velocity estimate. Simply increasing the S/STD threshold was also found to reduce the estimation error, with the possible risk of excluding useful data.

[65] In some cases, implementing this quality control can greatly increase the acceptable number of pairs above the S/STD threshold. For example, the data from PRN27 on 8 July 2000 is shown in Figure 16. The top plot shows the acceptable range of S/STD to be between 4.5 and 4.8 (a very narrow range), without the directional criteria. The bottom plot shows the increase of the acceptable range to be between 3.5 and 5.2 once the outliers are rejected by the QC boundary test. This gives a more robust estimate.

[66] We have identified two conditions that could yield such outliers. One is that the signal is simply too noisy. In that case, the measurement should have a low S/STD and be rejected by the threshold test. The second condition is that the cross-correlation function has more then one peak, as shown in Figure 17. The cross-correlation in Figure 17 has one peak at around a lag of −10 samples and another one at around a lag of

50 samples. Thus an incorrect value of Δt_i could be estimated due to this ambiguity.

[67] The QC boundary test can produce false detections, however, if a very narrowband filter is used. A sufficiently narrowband filter will produce nearly monochromatic signals even for an input of white noise. These monochromatic waves could appear to be coherent between pairs of stations. The method of section 2, however, requires the cross-correlation between many pairs of stations and a fitting of a single geometric model to this set of cross-correlations. The phases of each such monochromatic oscillation would change randomly with each station-pair. This would not agree with the assumed geometric model and would thus result in very large residuals.

[68] We generated simulated white noise time series and then input them to the detection algorithm using filters of different bandwidths. We found that no false detections occurred when the filter bandwidth was wider than 30 s. Rarely, false detections were found when a narrower bandwidth was used and the QC boundary was applied.

[69] It is thus possible that using the QC boundary test to select the data could have the effect of artificially introducing an apparent direction of propagation into random data. There are two precautions which could be taken to reduce this possibility. The first is to make a comparison between the results with and without the QC boundary test. Recall that the QC boundary test would only increase the acceptable threshold range and im-
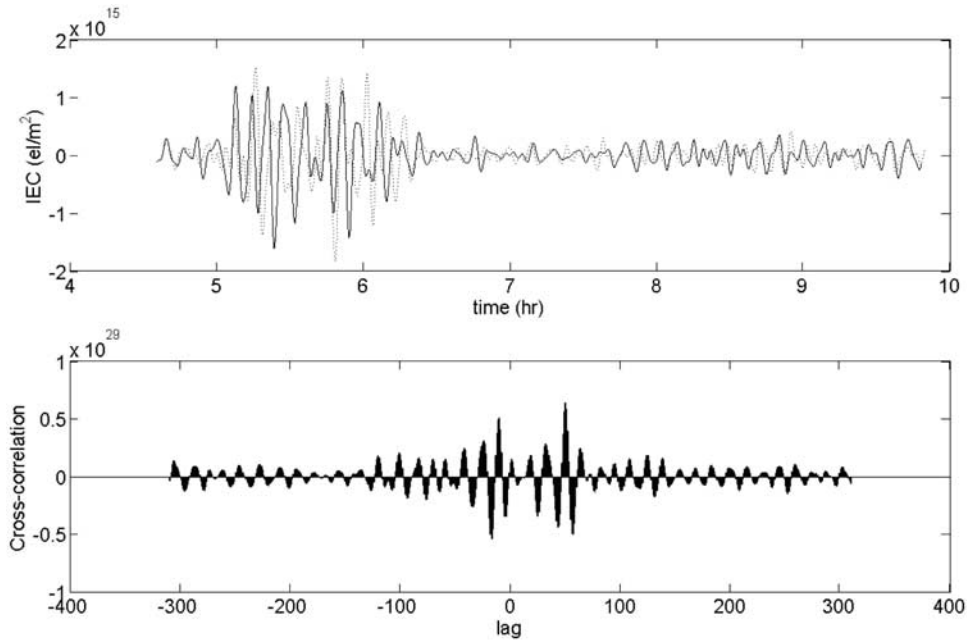
Figure 17. Example of an incorrect estimate of $\vec{V}_{ob}$ resulting from multiple peaks in the cross-correlation. (top) IEC time series from two GPS receivers. (bottom) Cross-correlation with two local peaks of nearly the same magnitude. PRN8 on 7 July 2000.

prove the estimation by providing a larger number of acceptable measurements, as shown in Figure 16. Therefore if there is no detection at any threshold without using the QC boundary, then the detection with the QC boundary is likely a false one. The other precaution is to use a wider bandwidth for the filter. The filter used for most of the work in this study (3–10 min) has a much larger bandwidth than that used to demonstrate the false detections.

4.5. Quality Control by Postfit Residuals

[70] The final quality control test that is applied in the estimator is the exclusion of Δt_i measurements that correspond to residuals greater than 2 standard deviations away from the mean. The pairs of Δt_i and $\Delta \vec{x}_i$ within these limits are retained and a second least squares estimate performed.

5. Results

[71] Four weeks of data were processed, one week in each season: summer (5–12 July 2000), fall (13–19 October 1999), spring (1–7 April 2001) and winter (1–7 January 2001). Data were not available for 9 July 2000. We limited the array size to stations concentrated in the Los Angeles region. This reduces the error in

propagation direction, as a result of the flat-Earth assumption, to less than 2 degrees. With this limitation, there were still 175 stations available with 30-s sampling.

[72] The estimated propagation velocities, midpoint times, and estimation statistics, for all of the disturbances detected during these four weeks, are presented in Tables 1–4.

[73] Figure 18 shows the results from 7 July 2000. The SIP trajectories are plotted, with heavy dots representing the locations of strong disturbances (amplitude of the filtered IEC exceeding 50% of its maximum). The estimated propagation velocities are drawn as vectors and the error ellipse of 4 STD is drawn to the same scale. (A 4 STD ellipse was used to make it visible when plotted on the same scale as the propagation velocity vector).

[74] One can see in Figure 18 that many of the estimated velocities are closely parallel to the local SIP direction of motion. This was found to be generally true for many of the disturbances that were detected. In order to test for a possible directional bias in the estimation method itself, we ran the simulation described in section 4.1 and varied the azimuth of the propagation vector in increments of 45°. We found no bias between the estimated direction and that of the simulated data. However, we found large (109%) estimation errors when the projected SIP velocity was very close to the propa-

Table 1. Summary of the Detections of Ionospheric Disturbances Within the 3–10 min Band for the Week of 13–19 October 1999

Day	PRN	Speed, m/s	Az., deg	Error, %	LT, h	95% CI Speed, m/s	95% CI Az., deg
13	5	339	−88	1.24	1.42	7.8	0.99
	6	105	−98	1.17	2.27	2.6	0.87
	7	92	−50	1.12	22.68	2.3	1.42
	10	68	−52	0.78	3.49	1.2	0.91
	17	84	−105	4.14	5.01	7.9	3.41
	21	135	−112	2.14	6.92	6.5	1.96
	23	98	−71	3.97	6.56	8.5	4.52
	24	125	−57	0.95	2.02	2.6	1.02
	25	257	109	2.98	9.57	14.7	3.64
	30	174	−110	4.59	0.46	19.2	4.73
14	1	661	−136	7.7	9.94	116.4	9.67
	6	104	−106	3.64	2.17	8.5	3.66
	21	413	−123	4.81	6.35	43.7	6.26
	23	309	−124	16.92	4.8	167.2	22.91
15	1	906	−142	12.83	9.83	302.2	16.17
	5	51	−111	6.21	22.74	8.1	7.01
	6	120	−125	13.25	1.04	46.7	17.72
16	1	869	−110	4.95	14.69	81	6.14
	5	95	−123	2.78	22.82	5.9	2.95
	6	373	−127	4.14	0.37	33.8	5.32
	17	633	−114	6.58	3.52	89.6	8.14
	21	751	−103	18.61	9.34	242	7.18
	23	558	−35	15.68	8.71	221.5	17.53
	24	228	−41	3.44	2.58	18.2	4.63
	26	518	175	9.25	3.03	110.7	5.15
	29	81	−37	3.47	10.75	6.7	4.59
17	1	457	−134	8.8	9.88	91.3	11.08
	7	63	−63	3.52	21.57	5.1	4.09
	14	355	−74	7.59	10.78	54.2	8.7
	21	977	−107	2.32	5.47	39.6	2.86
	23	356	−88	6.06	7.1 3	8.8	0.68
	25	213	122	14.55	8.99	80.4	20.67
18	1	766	−84	10.73	10	125.6	2.41
	5	279	−82	2.22	0.81	13.1	1.7
	19	692	−142	6.12	14.08	97.6	7.6
	23	239	−114	6.27	4.24	28.5	7.96
19	1	765	−107	4.97	10.29	65.2	6.15
	5	110	−104	2.28	23.47	5.6	1.84

Table 2. Summary of the Detections of Ionospheric Disturbances Within the 3–10 min Band for the Week of 5–12 July 2000

Day	PRN	Speed, m/s	Az., deg	Error, %	LT, h	95% CI Speed, m/s	95% CI Az., deg
5	8	102	−120	2.31	22.31	4.9	3.02
	21	200	−113	6.16	11.29	27.3	8.89
	27	89	−119	8.63	21.92	20.3	12.74
6	27	159	−115	6.27	21.71	23.6	7.70
7	1	473	−30	8.27	21.89	92.6	9.38
	2	145	−113	3.47	23.95	11.2	3.87
	4	55	−130	4.86	2.83	6.3	6.42
	8	93	−92	2.03	23.50	3.4	1.78
	17	896	−111	5.15	7.89	89.5	6.35
	19	88	−54	3.74	22.77	7.5	4.51
	27	100	−83	5.48	22.45	10.8	5.49
8	1	707	−91	7.38	19.24	85.6	1.06
	27	204	−89	19.07	23.69	79.7	7.72
10	1	164	−117	6.20	17.65	20.1	8.62
	5	**2978**	**−88**	**10.94**	**6.79**	**297.6**	**1.43**
	8	132	−108	3.35	22.47	9.0	3.96
	17	1832	−48	27.21	12.00	2015.9	35.13
	19	1606	−97	18.06	20.09	373.1	5.09
11	1	996	−104	3.41	18.24	62.6	4.14
	5	**2038**	**−80**	**5.74**	**7.80**	**181.4**	**6.80**
	6	1928	−90	5.13	11.15	113.7	0.37
	8	1458	−102	6.41	21.44	178.3	7.34
	15	850	−82	3.60	14.81	51.2	4.02
	19	1723	−89	5.79	19.39	146.7	0.57
	27	**2078**	**−91**	**3.71**	**20.29**	**84.7**	**0.20**
	30	1797	−83	8.48	8.76	234.6	1.77
12	**3**	**2257**	**−42**	**18.11**	**13.66**	**1038.8**	**21.53**
	6	1451	−108	28.23	10.74	768.8	13.38
	8	215	−119	9.15	21.78	49.8	12.10

gation velocity. This case represented a degenerate geometry in which the SIP trajectory nearly follows the wavefront of the disturbance. The IEC measurement would therefore show little variation. When the simulation was repeated using a higher speed (300 m/s) disturbance, the estimation error decreased from 109% to 10.8% for the worst case. We therefore conclude that the geometric model and inversion method themselves do not introduce a systematic bias that favors propagation velocities parallel to the SIP motion. The Doppler-like effect, as described in section 4.1, may contribute to the directional bias, as could the "phase cancellation effect," described in the discussion section.

Table 3. Summary of the Detections of Ionospheric Disturbances Within the 3–10 min Band for the Week of 1–7 January 2001

Day	PRN	Speed, m/s	Az., deg	Error, %	LT, h	95% CI Speed, m/s	95% CI Az., deg
1	15	1528	−105	10.47	22.94	262.6	13.70
	17	424	−129	0.64	2.97	5.9	0.83
	21	**3441**	**−75**	**8.71**	**0.06**	**428.4**	**11.03**
2	5	107	−101	4.92	23.40	12.1	3.53
3	5	110	−101	4.26	23.46	10.6	3.28
4	23	1607	−86	2.86	22.52	62.2	3.29
6	7	158	159	6.55	11.71	24.8	5.50
	15	1696	−75	3.21	1.31	98.2	3.83
7	6	1966	−87	3.38	22.35	68.8	0.22
	17	**3202**	**−77**	**26.13**	**0.49**	**1013.6**	**8.23**
	21	925	−79	11.43	2.86	242.6	12.10
	23	431	−59	5.16	0.80	60.6	7.28
	29	1519	−80	8.15	1.31	280.4	7.12

Table 4. Summary of the Detections of Ionospheric Disturbances Within the 3–10 min Band for the Week of 1–7 April 2001

Day	PRN	Speed, m/s	Az., deg	Error, %	LT, h	95% CI Speed, m/s	95% CI Az., deg
1	1	1746	−119	1.09	23.51	35.3	1.39
	2	568	−128	8.01	4.46	92.3	10.02
	10	174	−156	16.52	12.50	81.0	13.49
	13	403	−19	5.02	5.21	46.3	4.17
	14	70	−177	1.69	18.50	2.7	0.45
	20	392	−8	0.73	2.33	6.4	0.38
	27	137	−7	16.05	6.88	57.9	10.73
	28	357	180	2.07	0.28	15.4	1.09
	30	75	−25	6.18	14.58	11.3	5.35
2	1	532	−124	1.65	23.51	17.5	2.11
	13	333	30	14.74	4.99	119.0	13.79
	20	401	−14	3.18	2.13	28.0	2.78
	25	275	−164	2.33	20.57	14.3	2.08
	28	213	−162	0.87	0.31	4.2	0.61
3	1	95	−98	6.35	23.89	14.0	3.87
	2	290	−135	11.66	4.39	94.7	16.60
	8	520	−108	6.55	3.07	68.5	7.77
	13	209	−81	5.41	1.45	17.4	6.51
	20	197	30	1.93	2.05	8.6	2.10
	27	312	−110	7.78	2.38	47.0	9.66
4	1	151	−102	1.00	0.41	3.1	0.95
	13	142	−108	1.54	1.36	4.8	1.58
	25	337	157	2.25	20.64	16.2	2.65
	27	270	−99	3.43	3.54	17.5	3.53
5	1	101	−111	3.46	0.16	7.9	3.48
	2	440	−116	8.99	5.20	81.9	11.37
	4	314	−176	8.53	8.21	62.4	4.39
	6	724	−161	1.31	12.32	21.0	1.21
	7	67	−132	1.45	6.35	2.2	1.88
	8	164	−144	1.69	2.94	6.2	1.97
	13	116	−100	2.60	1.47	6.2	2.30
	14	83.	−49	4.52	21.84	9.1	6.02
	25	344	159	2.48	20.64	17.7	2.98
	27	271	−100	3.96	3.56	20.4	4.15
6	2	351	−126	0.61	4.86	4.4	0.78
	8	106	−125	6.46	3.37	16.0	8.23
	13	161	−121	4.32	0.61	15.6	5.41
	14	305	−68	10.56	17.75	62.2	13.66
	27	228	−121	7.32	2.32	37.7	9.14
	28	41	−152	14.79	0.28	18.1	18.67
7	1	545	−108	3.39	23.14	29.8	4.29
	2	233	−148	1.20	4.46	6.0	1.12
	8	428	−131	2.60	2.74	24.0	3.31
	10	617	177	5.15	13.72	66.0	3.41
	13	1029	−39	12.84	4.42	305.0	14.59
	24	566	−171	16.79	13.00	239.6	18.25
	27	234	−141	1.20	1.72	6.0	1.32

[75] We found a few exceptional cases in July 2000 and January 2001 in which the estimated speeds were above the speed of sound in the ionosphere (>2000 m/s). These cases are labeled in bold in Tables 1–4. The TDI maps of two such cases are shown in Figure 19, in which the slopes of the coherent color patterns are close to vertical. We propose that these disturbances were not propagating waves, but rather some form of instantaneous disturbance to the ionosphere, possibly from an extraterrestrial source. Solar flares have been shown to induce a nearly instantaneous disturbance to a large area of the ionosphere which can be observed in IEC measurements [*Afraimovich*, 2000].

[76] Table 5 compares the times of six instances in which the estimated velocity exceeded 2000 m/s to the nearest time for solar X-ray flares detected by the GOES satellite (http://www.ngdc.noaa.gov/stp/SOLAR/flareint.html). The midpoint times of four of these occurrences were within 30 min of the maximum of a solar flare. As a reference, the median time between solar flares for each year and month in Table 5 are also included. From this limited set of data, it appears plausible that the events observed on 10 July 2000 (PRN 5) and the event on 12 July 2000 (PRN 3) were caused by solar flares since the flare and the ionospheric disturbance were much closer in time than the median separation between solar flares (which can be interpreted as the approximate time that random events could be correlated with the flares). These two disturbances also occurred on the day side of the Earth (local times (LT) of 7 H 48 M and 13 H 40 M, respectively). The disturbance found on 11 July 2000 (PRN 5) was most likely not caused by a solar flare, as it was not observed until more then 2 hours after the closest flare. The remaining three events are questionable, since they did occur within an hour of a solar flare, which quite probably was a coincidence, but were not on the daylight side of the Earth.

6. Conclusions and Discussion

[77] We have demonstrated a method to detect short period propagating disturbances in the ionosphere using IEC time series from a network of GPS stations. The propagation speed was determined with a precision better than 25% (error% in Tables 1–4). The 95% confidence interval in direction is 35° for the worst case and below 10° in most cases.

[78] In the 28 days of data that were processed, 127 disturbances were clearly identified by their presence on more than 10 pairs of stations. The signals were found to be coherent over large-areas (up to 1000 km), although their sources are still not understood. The horizontal component of the propagation velocity was found to range from around 50 to 1000 m/s, spanning the range of both gravity and acoustic waves. The velocity is measured with respect to an Earth-centered-Earth-fixed reference frame, therefore the velocity of a nonstationary ionosphere will also contribute some portion to the estimated velocity vector. This method is incapable of measuring the vertical component of the propagation velocity, therefore a large variations of the measured
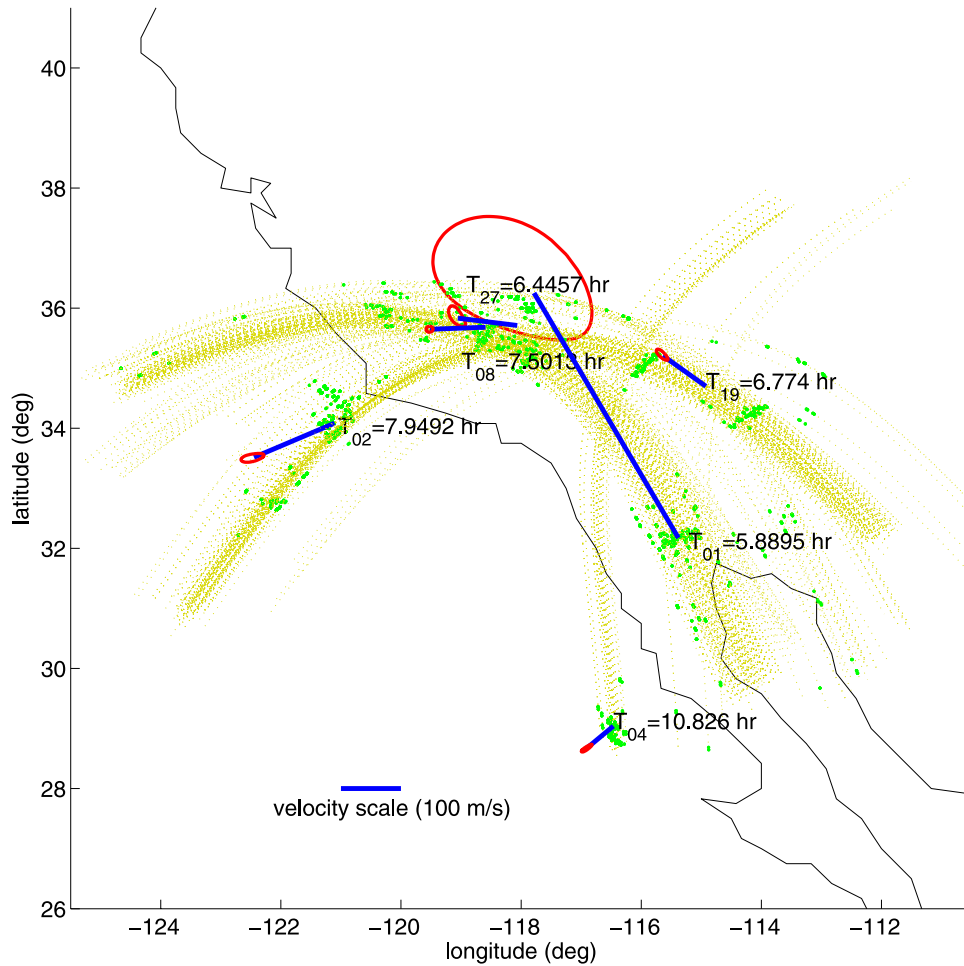
Figure 18. Map of the estimated velocity (7 July 2000), time and the location of detections at the west coast. The ellipses indicate the range of 4 standard deviations on the same scale as the velocity vector.

velocity, due to the uncertainty of the elevation of the propagation direction, is possible. The presence of upper atmosphere winds, and the aforementioned Doppler-like effect would change the apparent frequency and velocity of the waves.

[79] The Doppler-like effect, described in section 4.1 has been shown to substantially change the detectability of disturbances, through shifting the dominant frequencies outside of the filter passband. This effect could contribute to a directional bias since the frequency shift depends upon the component of propagation velocity in the direction of the SIP velocity. The resulting frequency change, however, will only shift the wave to a higher or lower frequency, so that it should be detected through a change in the bandwidth of the filter. This effect could only produce a directional bias if the most likely disturbances were within a narrow band of frequencies and

thus only the frequency shift resulting from motion aligned with the SIP would put them within the bandwidth of the filter.

[80] *Georges and Hooke* [1970] identified directional biases inherent in any measurement of perturbations in the ionosphere which are based upon IEC. Equation (9) in that reference describes the response of the IEC to a propagating wave disturbance in electron density, described by a general model that could represent either gravity or acoustic waves. That equation contains a product of three factors that describe this sensitivity. The first factor represents the fact that electrons can only be perturbed in directions parallel to the magnetic field (unit vector $\hat{b}$). The second factor describes a geometric bias term containing the vector product $(\hat{r} \times \hat{b}) \times \hat{z} \cdot \vec{k}$, in which $\hat{r}$ is the line of sight unit vector to the satellite, $\hat{z}$ is the vertical unit vector, and $\vec{k}$ is the wave propagation

Table 5. Comparison of High Speed ($\geq$2000 m/s) Ionospheric Disturbances With Solar

Flare Events Detected by X-Ray Measurements on the GOES Satellites						
Day	10 Jul 2000	11 Jul 2000	11 Jul 2000	12 Jul 2000	1 Jan 2001	7 Jan 2001
PRN	5	5	27	3	21	17
Speed, km/s	3.0	2.1	2.1	2.3	3.4	3.2
Time, LT	6 H 47 M	7 H 48 M	20 H 17 M	13 H 40 M	0 H 4 M	0 H 29 M
Flare start, LT	6 H 16 M	4 H 12 M	20 H 55 M	13 H 37 M	23 H 31 M[a]	0 H 34 M
Flare max., LT	6 H 26 M	5 H 10 M	21 H 2 M	13 H 40 M	23 H 35 M	0 H 40 M
Flare end, LT	6 H 37 M	5 H 35 M	21 H 9 M	13 H 43 M	23 H 39 M	0 H 47 M
Delay (from max)	21 M	158 M	−45 M	0 M	29 M	−11 M
Flare X-ray Class	M	X	M	M	C	C
Integrated Flux, J/m^2	1.3×10^{-2}	3.1×10^{-1}	8.8×10^{-3}	5.7×10^{-3}	4.3×10^{-2}	1.3×10^{-3}
Median time between flare maximums:						
Month	2 H 3 M	2 H 3 M	2 H 3 M	2 H 3 M	3 H 10 M	3 H 10 M
Year	2 H 12 M	2 H 12 M	2 H 12 M	2 H 12 M	2 H 4 M	2 H 4 M
Median time between flares:						
Month	1 H 50 M	1 H 50 M	1 H 50 M	1 H 50 M	2 H 47 M	2 H 47 M
Year	1 H 50 M	1 H 50 M	1 H 50 M	1 H 50 M	1 H 44 M	1 H 44 M

[a]31 December 2000.

vector. This defines a somewhat complex relationship between the propagation direction ($\hat{k}$), observation geometry ($\hat{r}$, $\hat{z}$) and magnetic field ($\hat{b}$). One instance in which this term would vanish is the case of $\hat{r}$ aligned with $\hat{b}$. In that scenario, electrons could only be perturbed along the line of sight, thus producing no change in IEC. The third factor takes the form of a Fourier transform of the electron density profile with a transform variable proportional to $\vec{k} \cdot \vec{r}$. This term accounts for the

"phase cancellation effect", in which depletion of electrons at one point along the line of sight is replaced by accumulation of electrons at another point, tending to reduce the net effect of the perturbation on the IEC. Numerical computations in that paper, done using a variety of different electron profiles, showed that this effect will strongly attenuate the IEC response of most disturbances, except for those within a narrow range of propagation directions for which $\vec{k} \cdot \vec{r}$ is near zero.
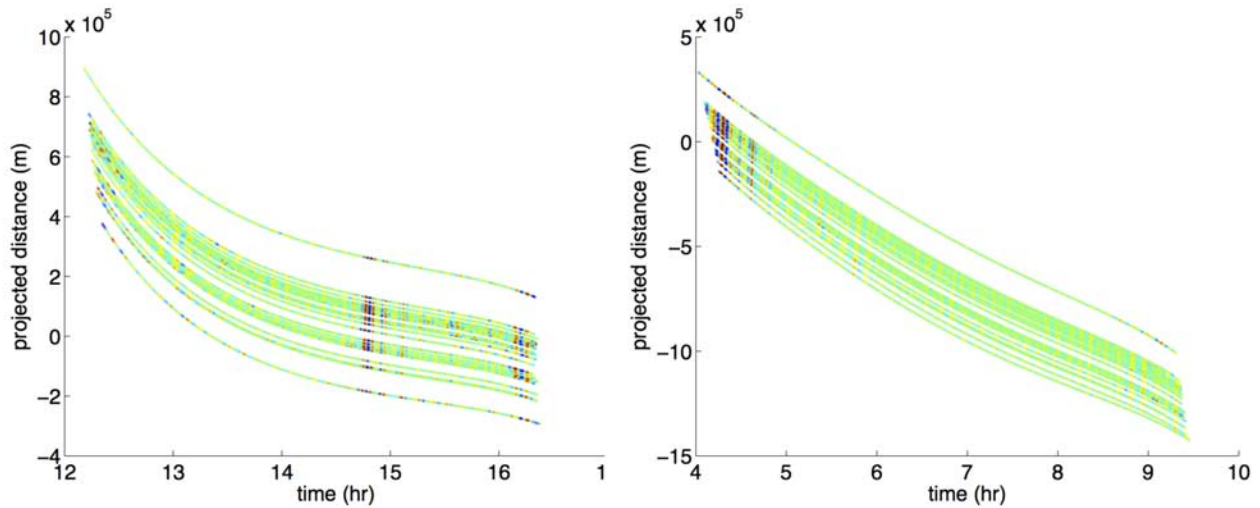

Figure 19. The TDI plot of two cases with high estimated velocities. (left) PRN5, 10 July 2000 ($\approx$3 km/s). (right) PRN27, 11 July 2000 ($\approx$2 km/s).

Afraimovich et al. [2001a, 1998] used this narrow range of sensitivity of the IEC change to the wave propagation direction to estimate the elevation of the wave using only knowledge of the azimuth.

[81] *Mercier and Jacobson* [1997] present similar results on the observational biases, expressing the efficiency of perturbations in the electron density ($n_{el}(l)$) at changing the IEC as the ''coherence factor''

$$f_{coher} = \frac{\left| \int n_{el}(l)dl \right|}{\int |n_{el}(l)|dl} \qquad (20)$$

[82] Both of these references arrive at the conclusion that these observational biases must be considered when using IEC measurements to derive statistics on the occurrence and propagation properties of ionospheric disturbances. *Georges and Hooke* [1970] further states that the variation in IEC amplitude, as a result of satellite motion, could modulate the IEC signal received at different ground stations differently, concluding that a detection test based upon correlation between measurements at different stations could be biased in favor of selecting disturbances that travel roughly parallel to the satellite trajectory. This hypothesis agrees with our findings. However, the variation in IEC due to differences in the phase cancellation effect between satellites might fall outside of the 3–10 min bandwidth. Further work is necessary to understand these biases, prior to any statistical study of the occurrence rates for these disturbances. Our cross-correlation method may fail to correctly estimate the propagation velocity if multiple waves were present. In *Afraimovich et al.* [1998], simulations of the SADM-GPS method, using a sum of two waves, showed that the best fit of a single-wave model to the data produced a result which amounted to approximately the intermediate speed and direction of propagation. This result, however, had a very low ''contrast''.

[83] We have demonstrated that disturbances in the 3–10 min bandwidth are more prevalent than previously thought. Previous investigations of disturbances of this type [*Afraimovich et al.*, 2003] were only capable of detecting individual, relativity large, disturbances such as the magnetic storm of 18 October 2001.

[84] The detected disturbances appear to be quite distinct from the more commonly observed traveling ionospheric disturbances (TIDs). Medium-scale traveling ionospheric disturbances are known to occur quite frequency, with certain preferred directions. These disturbances are understood to be the response of the ionosphere to gravity waves in the upper atmosphere [*Hines*, 1960; *Hocke and Schlegel*, 1996]. Models [*Mercier and Jacobson*, 1997] and experiments [*Yakovets*

et al., 1999; *Bristow and Greenwald*, 1996; *Galushko et al.*, 1998; *Bertin et al.*, 1975] both have shown that these disturbances propagate at lower speeds (200 m/s or less) and have longer periods (15 to 60 min) than most of the perturbations reported by *Calais et al.* [2003] or described in this paper. *Titheridge* [1968] found the most probable TID period is between 20 and 30 min, with a sharp lower cutoff around 15 min. Therefore, it is not likely that the disturbances that we observed, or those found in *Calais et al.* [2003], were manifestations of precisely the same phenomenon as the TID observations cited above.

[85] In addition, medium-period and short-period disturbances that have been reported in the literature arise from different physical causes. Short-period disturbances have been observed to be associated with acoustic waves and long-period disturbances have been assoicated with gravity waves.

[86] Finally, in section 4.4 we discuss the possibility that a very narrowband filter could introduce correlations between pairs of satellites for cases in which no coherent wave structure existed. Coupled with the QC boundary test, such a scenario was shown to have the potential to produce false detections of disturbances, which can be identified by large postfit residuals. The filters used to demonstrate the false detections also have a much narrower bandwidth (0.5 min) than any filter which has been used to process actual data.

[87] The method that we have developed has the potential to be used to characterize the occurrence of phenomena in the ionosphere in a more quantitative way, but only if the observational biases are understood and accounted for. Modeling of these observational biases should be the priority for future research on this problem.

[88] In the work presented in this paper, only measurements from the same satellite are processed within a single batch, although examples have been shown in which the same disturbance was detected in the signal of multiple satellites. The simultaneous processing of measurements from more than one satellite, fit to a single wave model, could lead to improved estimates and the reduction of some of these biases.

[89] We are not aware of any published statistics on the occurrence and properties of the shorter period disturbances, other than studies (described in the introduction) in which they were associated with specific impulsive events in the neutral atmosphere.

References

Afraimovich, E. L. (2000), GPS global detection of the ionospheric response to solar flares, *Radio Sci.*, 35, 1417–1424.

Afraimovich, E. L., K. S. Palamartchouk, and N. P. Perevalova (1998), GPS radio interferometery of travelling ionospheric disturbances, *J. Atmos. Sol. Terr. Phys.*, *60*, 1205–1223.

Afraimovich, E. L., E. A. Kosogorov, L. A. Leonovich, K. S. Palamartchouk, N. P. Perevalova, and O. M. Pirog (2000), Determining parameters of large-scale traveling ionospheric disturbances of auroral origin using GPS-arrays, *J. Atmos. Sol. Terr. Phys.*, *62*, 553–565.

Afraimovich, E. L., E. A. Kosogorov, N. P. Perevalova, and A. V. Plotnikov (2001a), The use of GPS arrays in detecting shock-acoustic waves generated during rocket launchings, *J. Atmos. Sol. Terr. Phys.*, *63*, 1941–1957.

Afraimovich, E. L., N. P. Perevalova, A. V. Plotnikov, and A. M. Uralov (2001b), The shock-acoustic waves generated by earthquakes, *Ann. Geophys.*, *19*, 395–409.

Afraimovich, E. L., N. P. Perevalova, and A. V. Plotnikov (2002), Registration of ionospheric responses to shock acoustic waves generated by carrier rocket launches, *Geomagn. Aeron.*, *42*(6), 755–762.

Afraimovich, E. L., N. P. Perevalova, and S. V. Voyeiko (2003), Traveling wave packets of total elevtron content disturbances as deduced from global GPS network data, *J. Atmos. Sol. Terr. Phys.*, *65*, 1245–1262.

Bertin, F., J. Testud, and L. Kersley (1975), Medium scale gravity waves in the ionospheric F-region and their possible origin in weather disturbances, *Planet. Space Sci.*, *23*(3), 493–507.

Blanc, E., and A. Jacobson (1989), Observation of ionospheric disturbances following a 5-kt chemical explosion: 2. Prolonged anomalies and stratifications in the lower thermosphere after shock passage, *Radio Sci.*, *24*, 739–746.

Bristow, W., and R. Greenwald (1996), Multiradar observations of medium-scale acoustic gravity waves using the Super Dual Auroral Radar Network, *J. Geophys. Res.*, *101*(A11), 24,499–24,511.

Calais, E., and J. B. Minster (1995), GPS detection of ionospheric perturbations following the January 17, 1994, Northridge earthquake, *Geophys. Res. Lett.*, *22*, 1045–1048.

Calais, E., and J. B. Minster (1996), GPS detection of ionospheric perturbations following a Space Shuttle ascent, *Geophys. Res. Lett.*, *23*, 1879–1900.

Calais, E., J. B. Minster, M. A. Hofton, and A. H. Hedlin (1998), Ionospheric signature of surface mine blasts from Global Positioning System measurements, *Geophys. J. Int.*, *132*, 191–202.

Calais, E., J. S. Haase, and J. B. Minster (2003), Detection of ionospheric perturbations using a dense GPS array in Southern California, *Geophys. Res. Lett.*, *30*(12), 1628, doi:10.1029/2003GL017708.

Ducic, V., J. Artru, and P. Lognonne (2003), Ionospheric remote sensing of the Denali Earthquake Rayleigh surface waves, *Geophys. Res. Lett.*, *30*(18), 1951, doi:10.1029/2003GL017812.

Fitzgerald, T. (1997), Observations of total electron content perturbations on GPS signals caused by a ground level explosion, *J. Atmos. Sol. Terr. Phys.*, *59*(7), 829–834.

Galushko, V. G., V. V. Paznukhov, Y. M. Yampolski, and J. C. Foster (1998), Incoherent scatter radar observations of AGW/TID events generated by the moving solar teminator, *Ann. Geophys.*, *16*, 821–827.

Georges, T. M., and W. H. Hooke (1970), Wave-induced fluctuations in ionospheric electron content: A model indicating some observational biases, *J. Geophys. Res.*, *75*, 6295–6308.

Hines, C. O. (1960), Internal atmospheric gravity waves at ionospheric heights, *Can. J. Phys.*, *38*, 1441–1481.

Hines, C. O. (1967), On the nature of traveling ionospheric disturbances launched by low-altitude nuclear explosions, *J. Geophys. Res.*, *72*, 1877–1882.

Hocke, K., and K. Schlegel (1996), A review of atmospheric gravity waves and travelling ionospheric disturbances: 1982–1995, *Ann. Geophys.*, *14*(9), 917–940.

Hudnut, K. W., Y. Bock, J. E. Galtetzka, F. H. Webb, and W. H. Young (2001), The Southern California Integrated GPS Network (SCIGN), paper presented at 10th FIG International Symposium on Deformation Measurements, Orange, Calif.

Jacobson, A. R., and R. C. Carlos (1994), Observations of acoustic-gravity waves in the thermosphere following Space Shuttle ascents, *J. Atmos. Terr. Phys.*, *56*(4), 525–528.

Kouba, J. (2003), A guide to using International GPS Service (IGS) products, Geod. Surv. Div., Ottawa, Ont., Canada.

Mannucci, A. J., B. D. Wilson, and C. D. Edwards (1993), A new method for monitoring the earth's ionospheric total electron content using GPS global network, paper presented at Conference GPS-93, Inst. of Navig., Salt Lake City, Utah.

Mannucci, A. J., B. D. Wilson, D. N. Yuan, C. H. Ho, U. J. Lindqwister, and T. R. Runge (1998), A global mapping technique for GPS-drived ionospheric total electron content, *Radio Sci.*, *33*, 565–582.

Mercier, C. R., and A. R. Jacobson (1997), Observations of atmospheric gravity waves by radio interferometry: are results biased by the observational technique?, *Ann. Geophys.*, *15*(4), 430–442.

Neter, J., M. H. Kutner, C. J. Nachtsheim, and W. Wassweman (Eds.) (1996), *Applied Linear Statistical Models*, 4th ed., McGraw-Hill, New York.

Otsuka, Y., et al. (2006), GPS detection of total electron content variations over Indonesia and Thailand following the 26 December 2004, *Earth Planets Space*, *58*, 159–165.

Titheridge, J. (1968), Periodic disturbances in the ionosphere, *J. Geophys. Res.*, *73*, 243–252.

Wolcott, J. H., D. J. Simons, D. D. Lee, and R. A. Nelson (1984), Observations of an ionospheric perturbation arising from the Coalinga earthquake of May 2, 1983, *J. Geophys. Res.*, *89*(A8), 6835–6839.

Yakovets, A. F., M. Z. Kaliev, and V. V. Vodyannikov (1999), An experimental study of wave packets in travelling ionospheric disturbances, *J. Atmos. Sol. Terr. Phys.*, *61*(8), 629–639.

J. L. Garrison and S.-C. G. Lee, School of Aeronautics and Astronautics, Purdue University, 315 N. Grant Street, West Lafayette, IN 47907, USA. (jgarriso@ecn.purdue.edu)

E. Calais and J. S. Haase, Department of Earth and Atmospheric Sciences, Purdue University, West Lafayette, IN 47907, USA.